Supporting Information

Single Atom Ir Doped Heterophase of NiMoP-NiMoP$_x$O$_y$ Ultrathin Layer Assembled on CNTs-Graphene/Cu for High-Performance Water Splitting

*Van Hien Hoa [a,b], Sampath Prabhakaran [a], Kha Thuy Nhi Le [a], Do Hwan Kim[b]**

[a]Department of Nano Convergence Engineering, Jeonbuk National University, Jeonju, Jeonbuk, 54896, Republic of Korea.

[b]Division of Science Education, Graduate School of Department of Energy Storage/Conversion Engineering, Jeonbuk National University, Jeonju, Jeonbuk 54896, Republic of Korea

*Corresponding author: Email (dhk201@jbnu.ac.kr)

Faradaic efficiency (η_F) calculation.

To evaluate the η_F of an electrolyzer during water splitting, evolved gases during water splitting were collected using a laboratory-made cell system. The volumes of evolved H_2 at the cathodic electrode and O_2 gas at the anodic electrode were measured by cylinders at 20 mA cm^{-2} for various time periods. The volumes of the theoretically evolved H_2 and O_2 gases were estimated using Faraday's law:

$$V_{Theo} = \frac{JRTt}{PzF} \quad \text{(S1)}$$

where V_{Theo} is the volume of the theoretically evolved gas, J is the operation current density (mA cm^{-2}), R is the ideal gas constant (R = 0.082), T is the operating temperature (K), t is the operation time period (s), P is the operation pressure (atm), z is the e$^-$number to produce 1 mol H_2 (z = 2) or 1 mol O_2 (z = 4), and F is Faraday's constant (F = 96,485 C).

η_F can be determined from the ratio of real gas (V_{Real}) to theoretical gas (V_{Theo}) evolving during the reactions.

$$\eta_F = V_{Real}/V_{Theo} \quad \text{(S2)}$$

DFT calculation.

DFT calculations were performed using the Vienna ab initio simulation package (VASP).[1] Generalized gradient approximation (GGA) in the form of the Perdew–Burke–Ernzerhof (PBE) functional and plane-waves up to an energy of 400 eV were used for the calculations.[2] A vacuum of over 16 Å was added to avoid artificial interactions between the slab and its images. The projector-augmented wave (PAW) potentials were used to describe the ionic potentials.[3,4]

Grimme's DFT-D3 van der Waals (vdW) correction based on a semi-empirical GGA-type theory was used to correct the dispersion forces.[5] The structures were allowed to relax until the Hellman-Feynman forces were smaller than 0.02 eV/Å. In the calculation of the density of states (DOS) and free energy the Γ-point-centered k-point meshes used for the Brillouin zone integrations were 2×2×2 and 4×4×1. The free energy change for H* adsorption was calculated based on the formula proposed by Norskov *et al*.:[6]

$$\Delta G_{H^*} = E_{H^*/surf} - E_{surf} - (E_{H2})/2 + \Delta E_{ZPE} - T\Delta S \qquad (S3)$$

where $E_{H^*/surf}$, E_{surf}, E_{H2}, ΔE_{ZPE}, and ΔS are the total energies of the slab with H*, clean surface, isolated hydrogen molecule, zero-point energy change, and entropy change, respectively.

Materials

Nickel (II) nitrate hexahydrate salt ($Ni(NO_3)_2 \cdot 6H_2O$, 98%), sodium molybdate dihydrate ($Na_2MoO_4.2H_2O$), 5 wt% Nafion solution, Pt nanoparticles (NPs) on graphitized carbon (Pt/C, 20% Pt on Vulcan XC72, Pt < 5 nm), sodium hypophosphite (NaH_2PO_2), and iridium (III) chloride hydrate ($IrCl_3.xH_2O$, 99.9%) were purchased from Sigma Aldrich Chemicals Co. (USA). Potassium hydroxide (KOH, ≥ 99.5%), ethanol (C_2H_5OH, 99.9%), hydrochloric acid (HCl, 35.0%-37.0%), and acetone (CH_3CHO, 99%) were purchased from Samchun Co. (Korea). Copper foam was purchased from Alfa Co. (USA). Argon, hydrogen, and methane gases were used as the carrier, reducing, and carbon source gases, respectively. Ultra-pure water, filtered using an EYELA Still Ace SA-2100E1 (Tokyo Rikakikai Co., Japan), was used throughout the experiments.

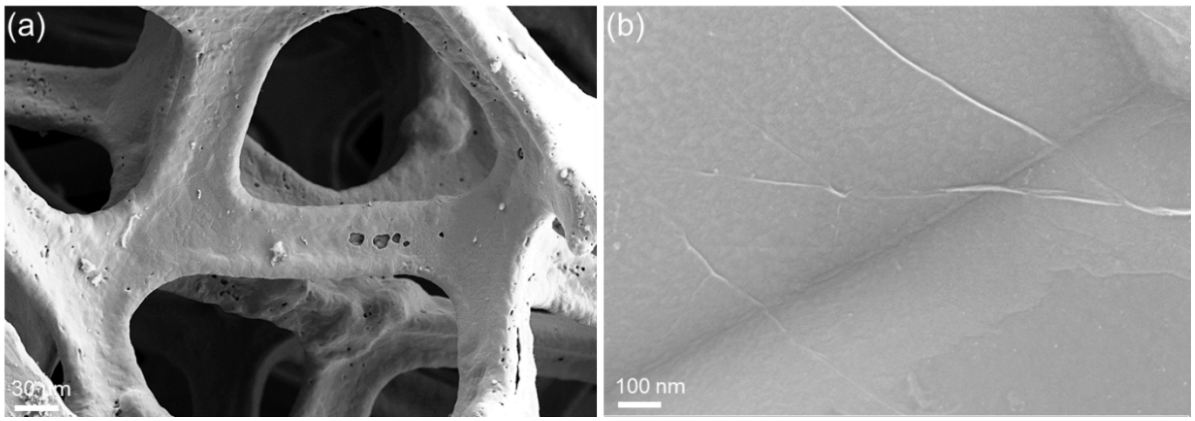

Fig. S1. SEM image of Gr/Cu, (b) HR-SEM of Gr/Cu.

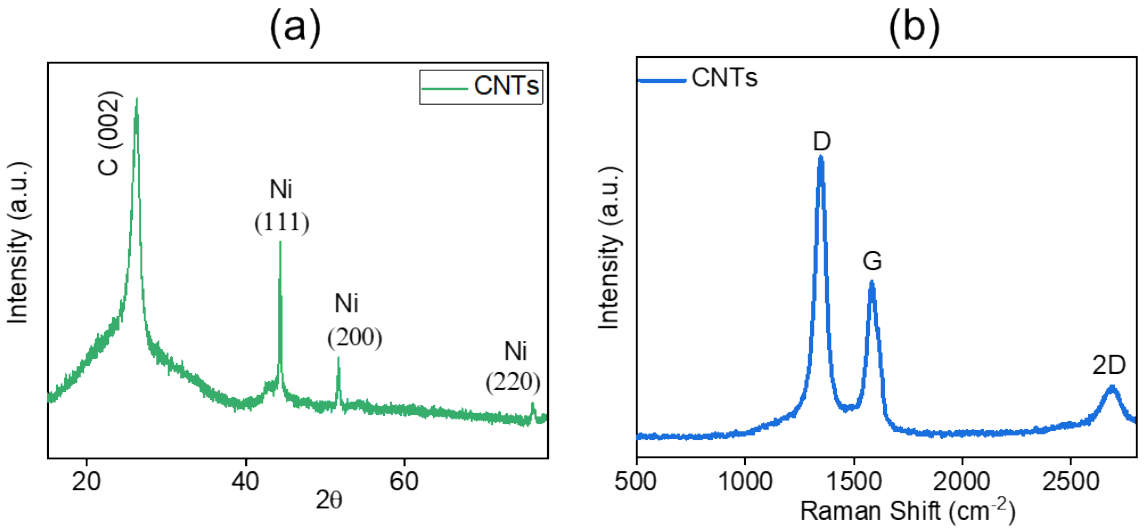

Fig. S2. (a) XRD pattern of CNTs, (b) Raman spectroscopy of CNTs.

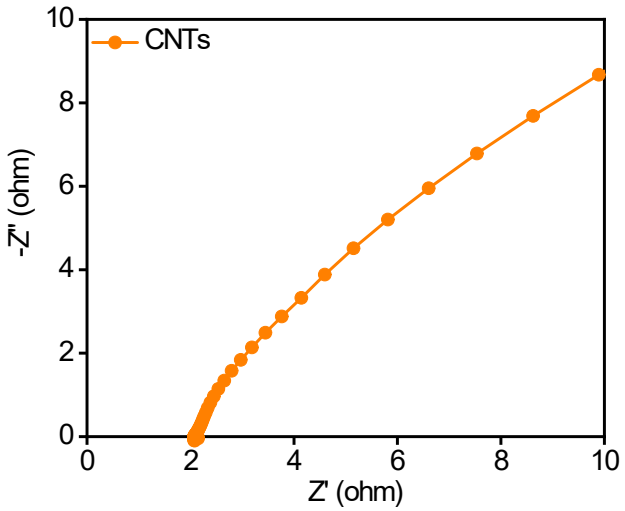

Fig. S3. Electrochemical impedance spectroscopy of CNTs-Gr/Cu.

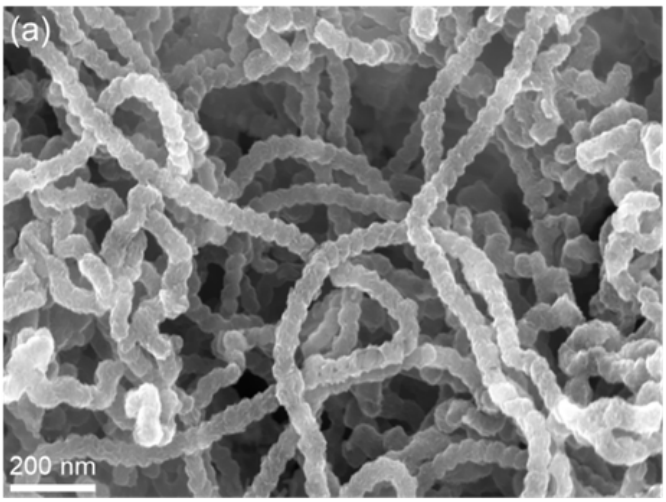

Fig. S4. (a) FE-SEM images of NiMo/CNTs-Gr/Cu.

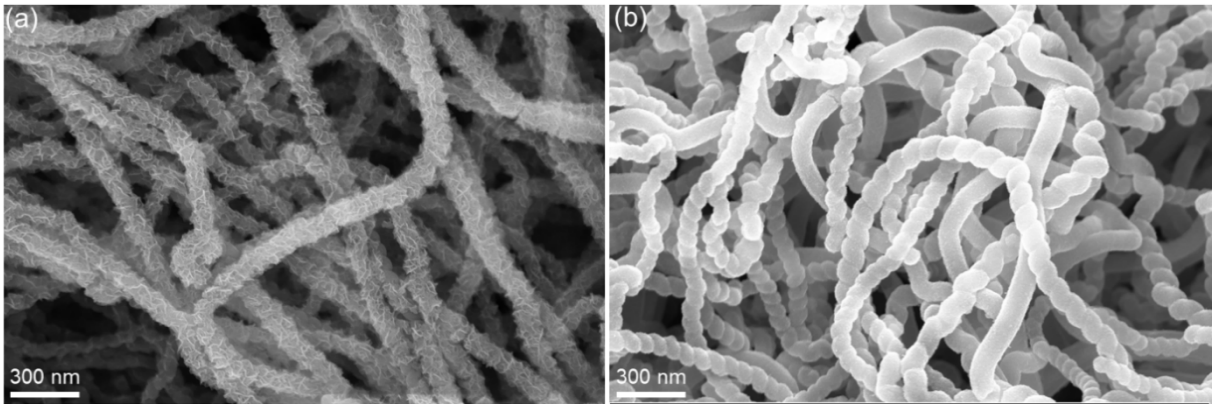

Fig. S5. (a) FE-SEM images of NiP-NiP_xO_y/CNTs-Gr/Cu, (b) MoP-MoP_xO_y/CNTs-Gr/Cu.

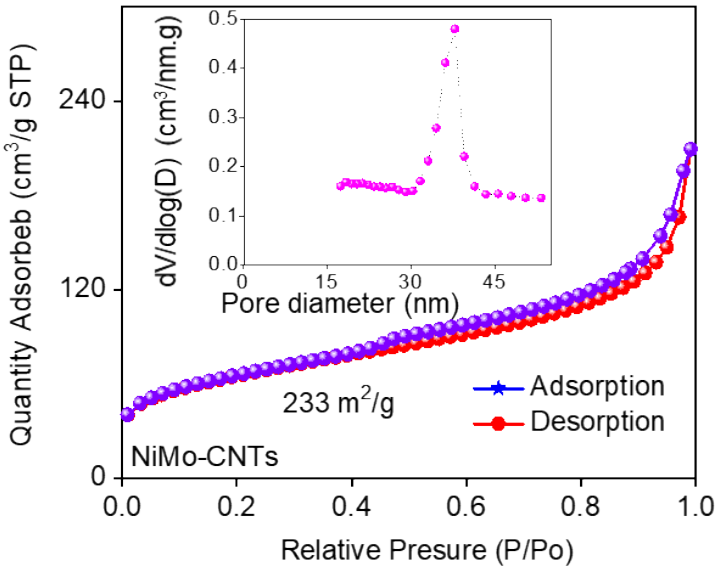

Fig. S6. Surface area and pore size and volume analysis of NiMo/CNTs-Gr/Cu.

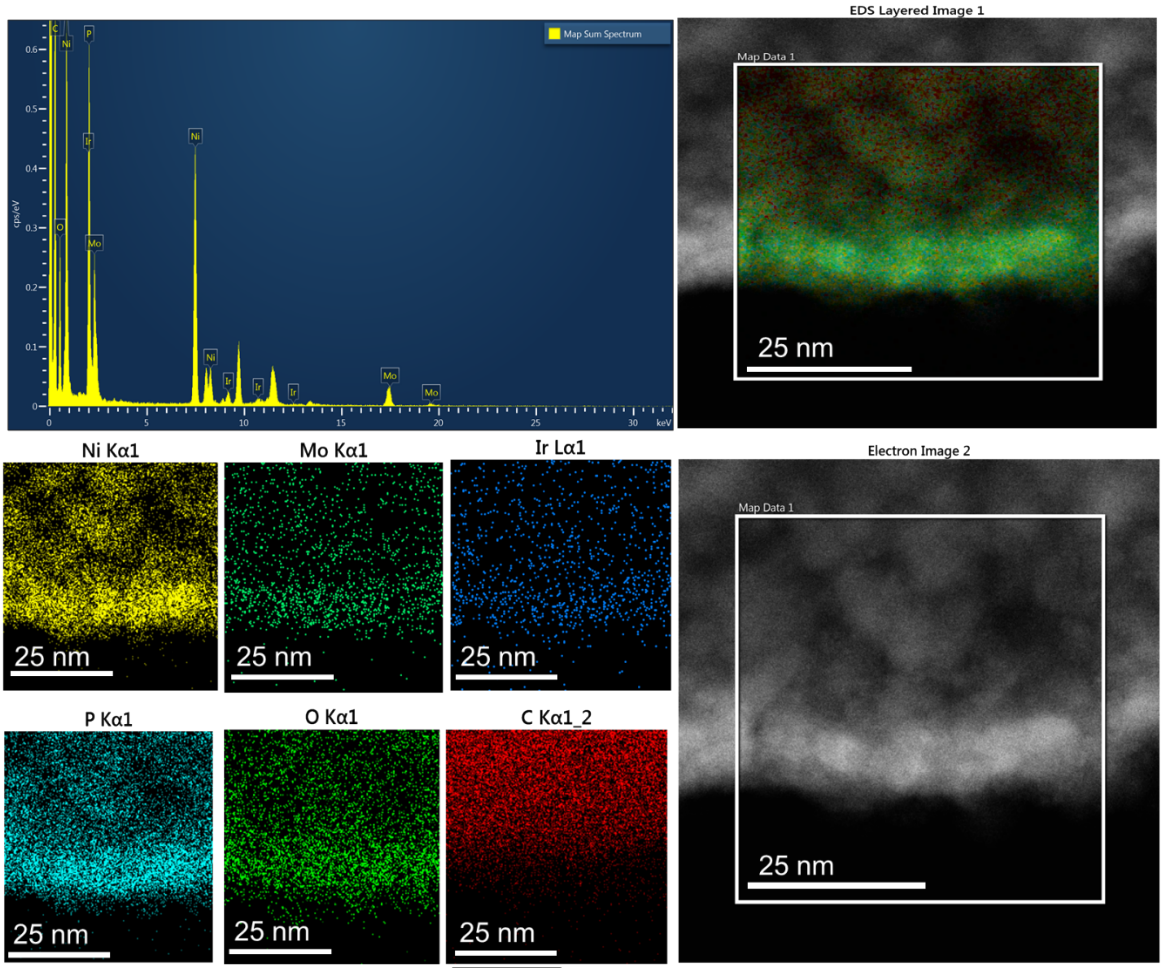

Fig. S7. STEM-EDS images of Ir-NiMoP-NiMoP$_x$O$_y$/CNTs-Gr/Cu.

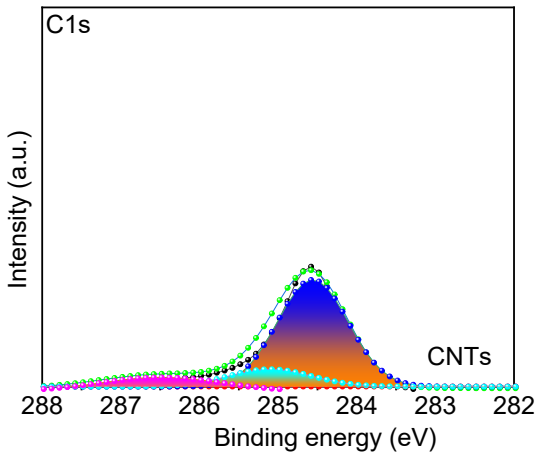

Fig. S8. High-resolution C1s of CNTs-Gr.

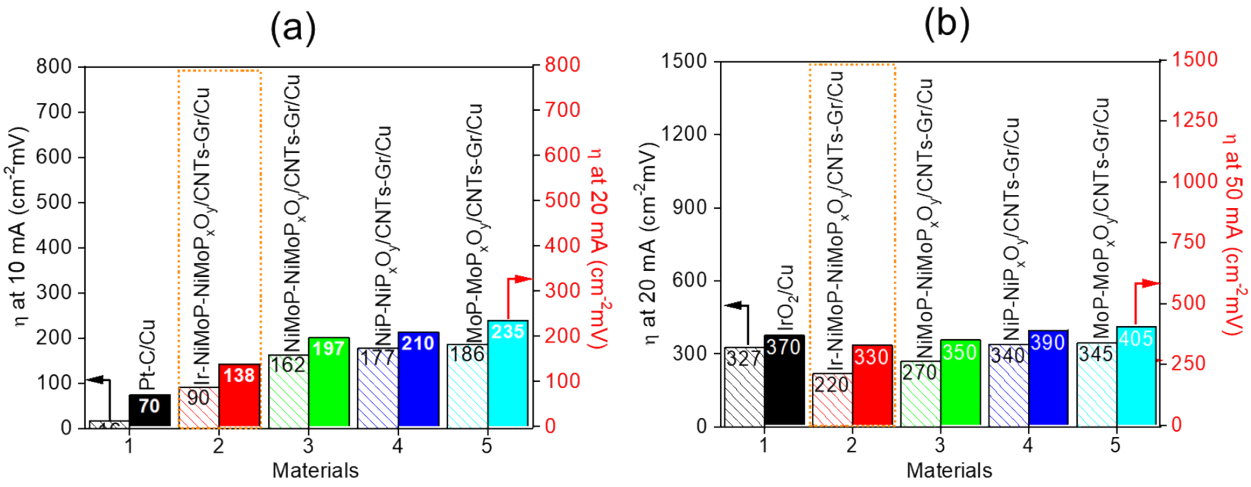

Fig. S9. (a) Overpotentials of HER at 10 and 20 mA cm^{-2}, (b) OER at 20 and 50 mA cm^{-2}.

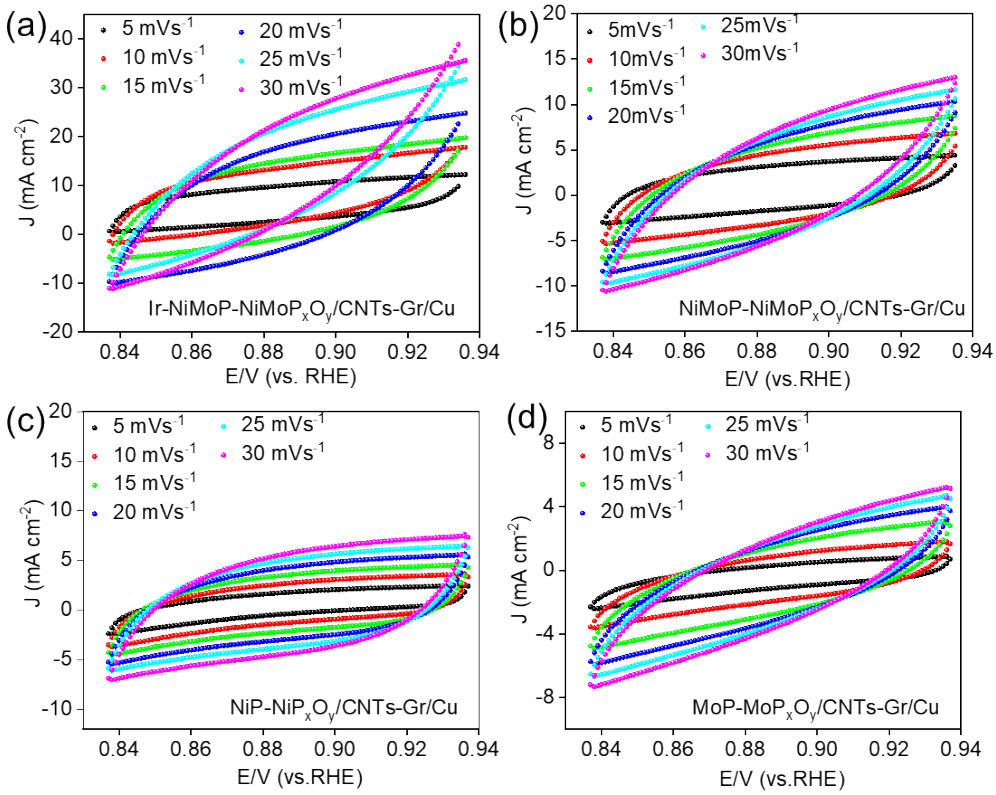

Fig. S10. CV at various scan rates of (a) Ir-NiMoP-NiMoP$_x$O$_y$/CNTs-Gr/Cu, (b) NiMoP-NiMoP$_x$O$_y$/CNTs-Gr/Cu, (c) NiP-NiP$_x$O$_y$/CNTs-Gr/Cu, and (d) MoP-MoP$_x$O$_y$/CNTs-Gr/Cu.

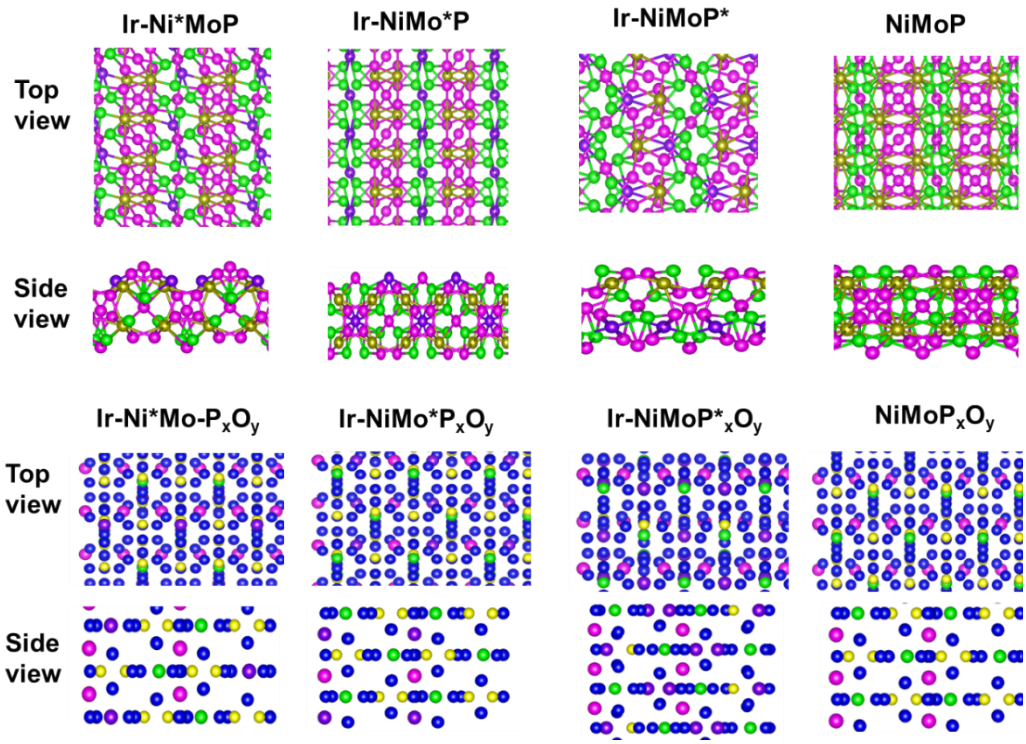

(*) *(position of the doping site)*

Fig. S11. Material models for DFT calculation of Ir-NiMoP, NiMoP, Ir-NiMoP$_x$O$_y$ and NiMoP$_x$O$_y$ materials.

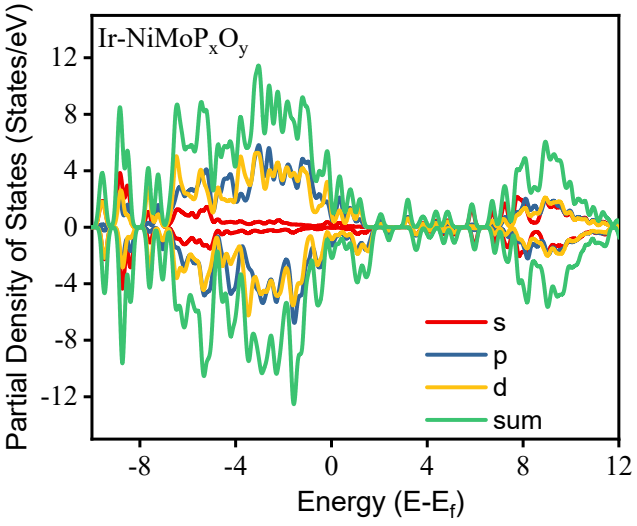

Fig. S12. The partial density of states (PDOS) of Ir-NiMoP$_x$O$_y$.

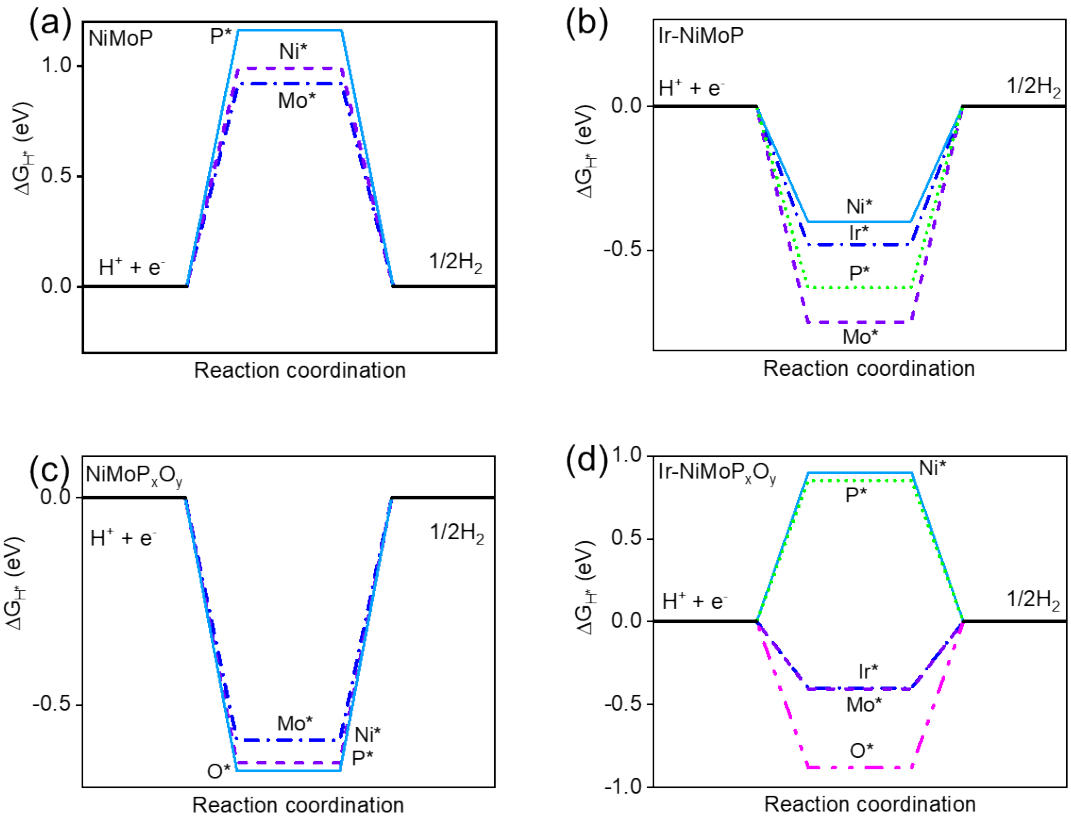

Fig. S13. ΔG_{H^*} of Ni, Mo, O, P, and Ni sites of (a) NiMoP, (b) Ir-NiMoP, (c) $NiMoP_xO_y$, (d) Ir-$NiMoP_xO_y$.

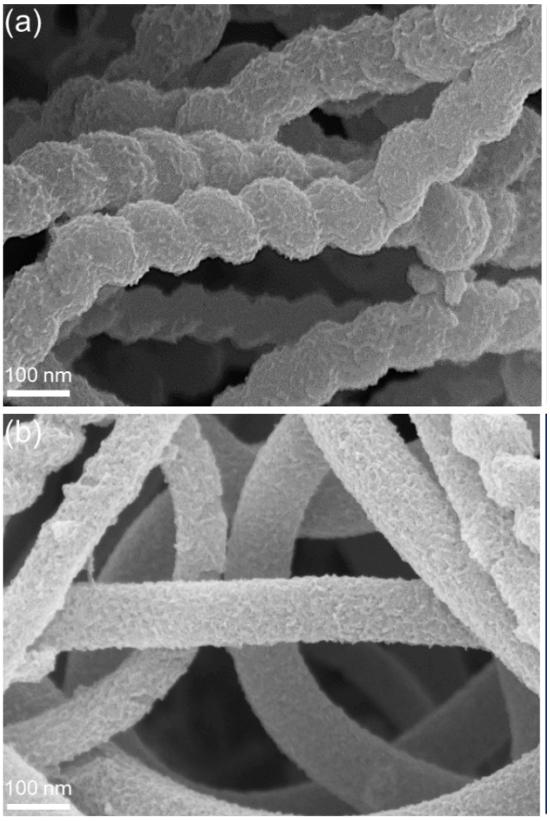

Fig. S14. SEM images of Ir-NiMoP-NiMoP$_x$O$_y$/CNTs-Gr/Cu with concentrations of (a) 0.01 mM and (b) 1 mM.

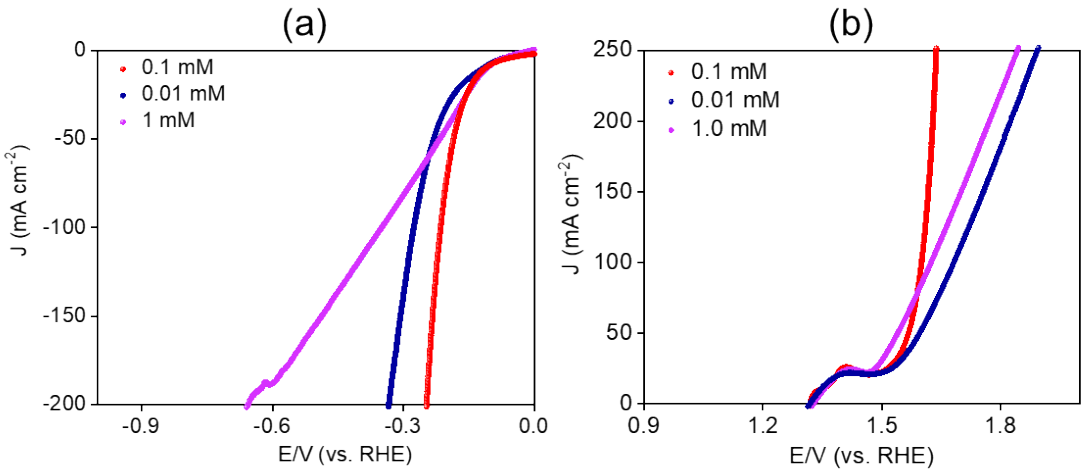

Fig. S15. (a) Linear sweep voltammetry of Ir-NiMoP-NiMoP$_x$O$_y$/CNTs-Gr/Cu with various concentrations of $IrCl_3$. xH_2O for HER and (b) OER.

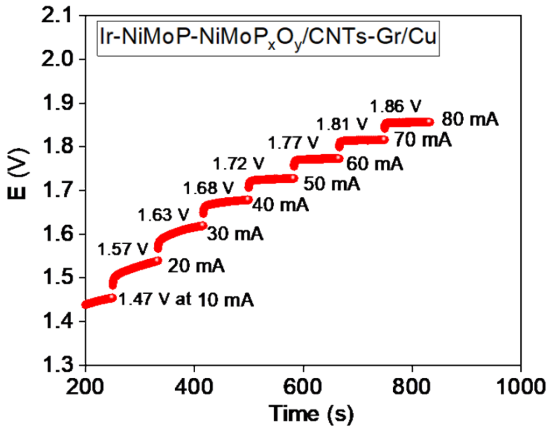

Fig. S16. Water electrolysis of Ir-NiMoP-NiMoP$_x$O$_y$/CNTs-Gr/Cu with different current density corresponding to energy density of batteries.

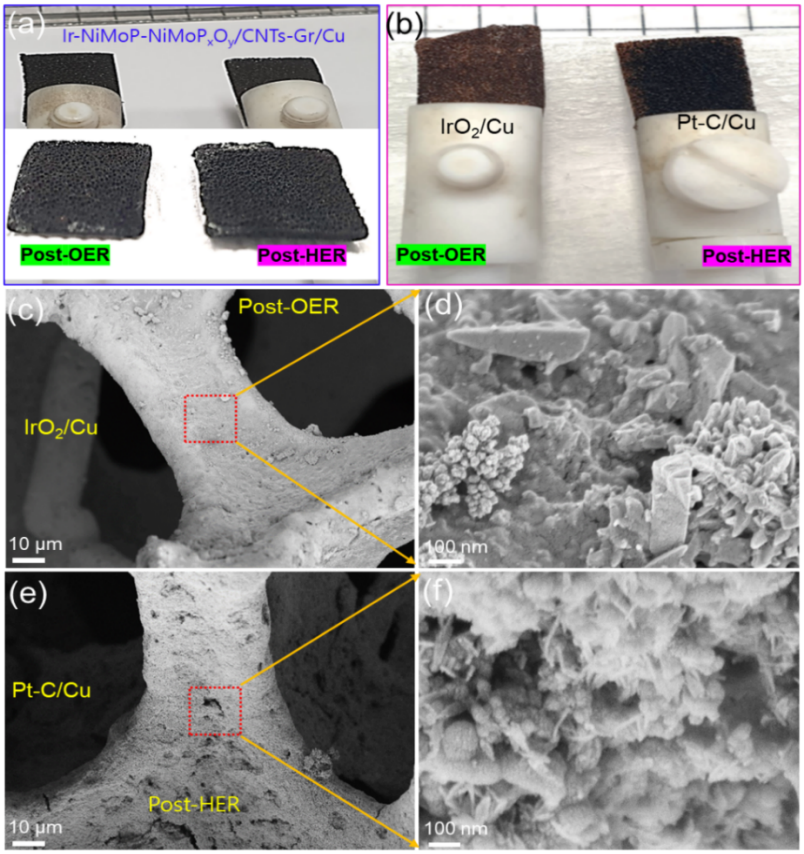

Fig. S17. (a) Photograph electrodes of Ir-NiMoP-$NiMoP_xO_y$/CNTs-Gr/Cu after stability testing, (b) images of IrO_2/Cu, Pt-C/Cu electrodes after stability, (c-d) morphology of IrO_2/Cu after stability testing, (e-f) morphology of Pt-C/Cu after post-HER.

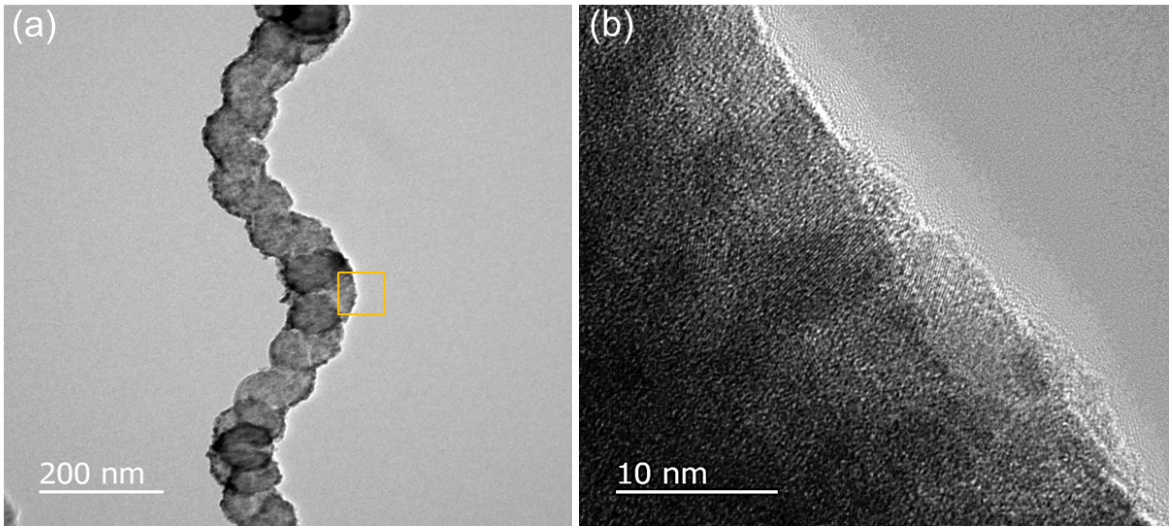

Fig. S18. (a) TEM, (b) HR-TEM image of post-HER.

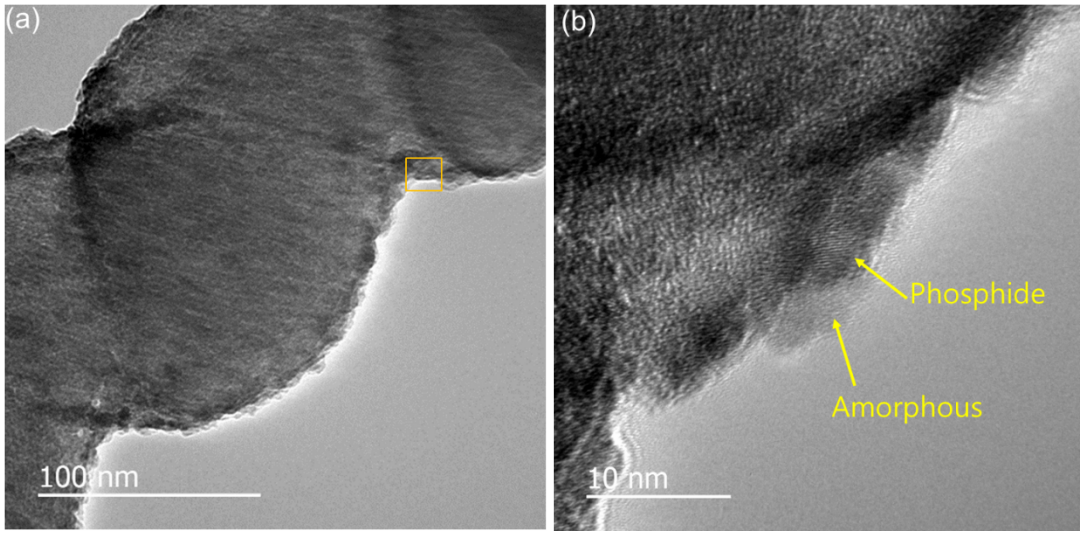

Fig. S19. (a) TEM, (b) HR-TEM image of post-OER.

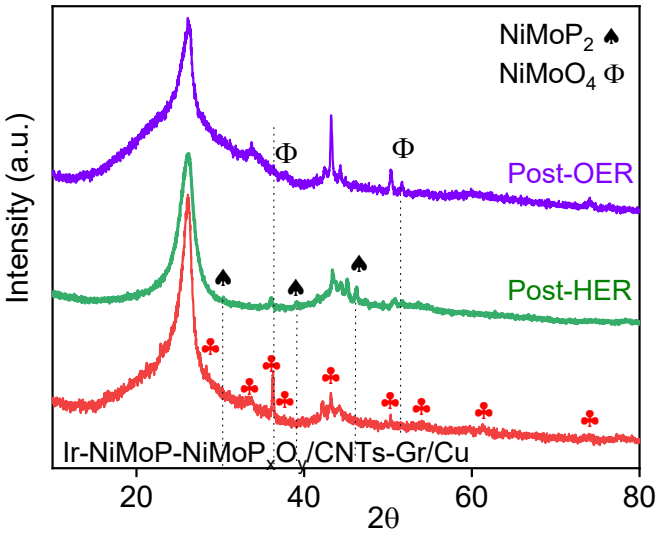

Fig. S20. XRD pattern of post-HER, post-OER and virgin sample of Ir-NiMoP-NiMoOPxOy/CNTs-Gr/Cu.

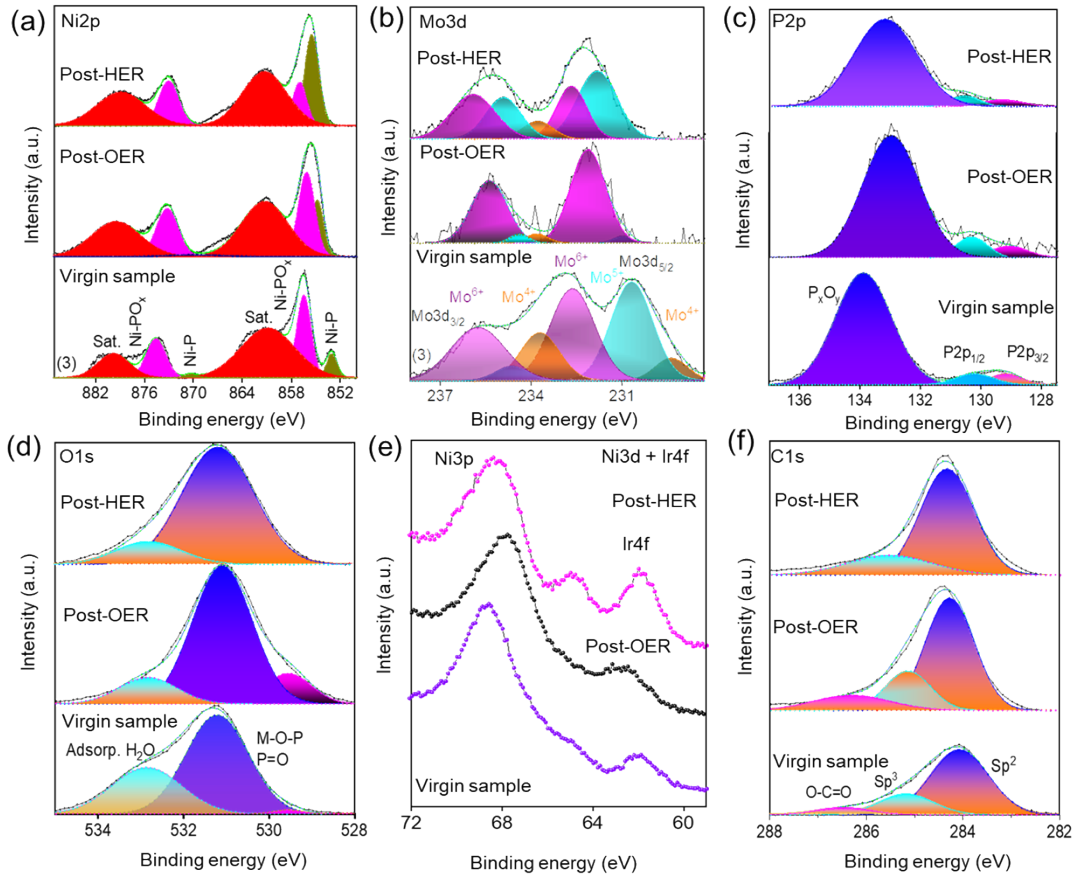

Fig. S21. High-resolution XPS of Ir-NiMoP-NiMoP$_x$O$_y$/CNTs-Gr/Cu: (a) Ni2P, (b) Mo3d, (c) P2p, (d) O1s, (e) Ir4f, and (f) C1s.

In the high-resolution Ni2p XPS spectra of Ir-NiMoP-NiMoP$_x$O$_y$/CNT-Gr/Cu of post-HER and -OER, there is an obvious increase in binding energy for the peak at approximately 856.6 eV, corresponding to oxidized Ni species (Fig. S21a). In addition, a higher intensity for the oxidized phosphate species can also be observed, confirming the oxidation of surface Ni and P. However, after the HER test, there is an intensity decrease at approximately 856.6 eV and an increase at approximately 854.4 eV, which can be attributed to the reduction of Ni species (corresponding to $Ni^{\delta+}$ in the Ni-P compound). Similarly, the high-resolution Mo3d spectrum (Fig. S21b) shows that the intensity of the Mo3d binding energy, as well as its Mo^{6+} components, significantly increased in the post-OER sample, implying an increase in oxidized Mo (Mo-O) states, which also originate from oxyhydroxides. These results indicate that the oxidation of the surface of the material related to Ni, Mo, and P synergistically boosted the electroactive surface area, adsorption energy, and the transmittance of electrons, thereby contributing to the OER activity. In addition, for more detail regarding the peak in HER, the high resolution of Mo3d was immediately obvious upon the reduction of Mo^{6+} to Mo^{5+} and a slight shift in the binding energies for MoO_3 and PO^{3-}_4, respectively. This caused a coupled lattice-electron distortion, which could potentially lead to enhanced electrochemical activity. For the P2p counterpart in Fig. S21c, the high-resolution P2p spectrum shows the lower binding energy peaks located at approximately 129.1 eV corresponding to the P2p line of NiMoP, and another contribution at approximately 133.8 eV that can be assigned to the oxidized phosphate species, with a slight reduction in the M-P intensity and an increase in the M-O-P and P=O intensities, which further confirmed the oxidation of NiMoP. The intense bands in the O 1s spectrum at 529.5 eV reveal abundant surface hydroxyls and oxygen from Ni and Mo oxides/hydroxides (Fig. S20d). In addition, the O1s spectrum of the post-OER sample had a higher intensity than the virgin one, and the O1s of HER at high resolution was consistent with an oxidation state decrease as well as modulation of the electronic structure or phase conversion for MoO_3 and P_xO_y because of the HER (Fig. S20e). These results verified the coexistence of Ir4f binding after stability, which was proof of stable Ir atoms in the heterophase, implying good strength for the Ir-NiMoP-NiMoP$_x$O$_y$/CNTs-Gr/Cu in terms of morphology and chemical structure, even after long-term HER and OER reaction. The carbon substrate tests were observed from the C1s spectrum (Fig. S21f).

Table. S1. ICP-MS of Ir in the Ir-NiMoP-$NiMoP_xO_y$/CNTs-Gr/Cu.

Samples	Sample amount (g)	Value dissolution (ml)	Ir (ppm)	Ir (wt%)
Ir-NiMoP-$NiMoP_xO_y$/CNTs-Gr/Cu	0.0264	50	1.075	~0.1

***** Sample preparation procedure

Ir: 1.075 ppm = 0.1% (1% = 10,000 ppm)

*1ppm = 1mg/L.

* Measurement of 1/10 dilution (multiplied by a dilution factor of 10 and inputting the sample amount of 0.0264 g and final volume of 50 ml, the concentration of the first powder is calculated as the result).

Table. S2. HER at 10 mA cm^{-2} with Ir-NiMoP-$NiMoP_xO_y$/CNTs-Gr/Cu and recently published materials

Catalyst	**Electrolyte**	**η of HER at 10 (mA cm^{-2})**	**Reference**
$Ni_{0.7}Fe_{0.3}S_2$	1.0 M KOH	155	[7]
Co-Mo_2C	1.0 M KOH	118	[8]
Ni-MoS_2	1.0 M KOH	98	[9]
Co/CoP	1.0 M KOH	138	[10]
MnNi	1.0 M KOH	360	[11]
Co-NRCNT	1.0 M KOH	370	[12]
MoB	1.0 M KOH	225	[13]
CoN_x/carbon	1.0 M KOH	170	[14]
O-CoP	1.0 M KOH	98	[15]
Co/CNT	1.0 M KOH	117	[16]
Co@NBC	1.0 M KOH	146	[17]
Co@N-CNTs@rGO	1.0 M KOH	108	[18]
Fe-Ni@NC-CNTs	1.0 M KOH	202	[19]
Ir-NiMoP-$NiMoP_xO_y$/CNTs-Gr/Cu	1.0 M KOH	90	This work

Table. S3. Comparison of OER at 20 mA cm^{-2} for Ir-NiMoP-$NiMoP_xO_y$/CNTs-Gr/Cu and materials reported in recent publications.

Catalyst	**Electrolyte**	**η of OER at 20 (mA cm^{-2})**	**Reference**
MnO/C	1.0 M KOH	329	[20]
Co/NBC	1.0 M KOH	490[#]	[17]
NiCoP	1.0 M KOH	330	[21]
NiCo LDH	1.0 M KOH	367	[22]
Co-P	1.0 M KOH	370	[23]
$MnNi_xO_y$	1.0 M KOH	450[#]	[11]
O-CoMoS	1.0 M KOH	286	[24]
NiCoS	1.0 M KOH	234	[25]
$NiFe_2O_4$	1.0 M KOH	329	[26]
$FeNi_3S_2$/FeNi	1.0 M KOH	330[#]	[27]
Ir-NiMoP-$NiMoP_xO_y$/CNTs-Gr/Cu	1.0 M KOH	220	This work

([#]) (*Value was calculated from the curves shown in the literature.)*

References

1 G. Kresse and J. Furthmüller, *Comput. Mater. Sci.*, 1996, **6**, 15–50.

2 J. P. Perdew, K. Burke and M. Ernzerhof, *Phys. Rev. Lett.*, 1996, **77**, 3865–3868.

3 Z. Huang, Z. Chen, Z. Chen, C. Lv, H. Meng and C. Zhang, *ACS Nano*, 2014, **8**, 8121–8129.

4 D. Joubert, *Phys. Rev. B - Condens. Matter Mater. Phys.*, 1999, **59**, 1758–1775.

5 S. Grimme, J. Antony, S. Ehrlich and H. Krieg, *J. Chem. Phys.*, , DOI:10.1063/1.3382344.

6 E. Skúlason, V. Tripkovic, M. E. Björketun, S. Gudmundsdóttir, G. Karlberg, J. Rossmeisl, T. Bligaard, H. Jónsson and J. K. Nørskov, *J. Phys. Chem. C*, 2010, **114**, 18182–18197.

7 J. Yu, G. Cheng and W. Luo, *J. Mater. Chem. A*, 2017, **5**, 15838–15844.

8 H. Lin, N. Liu, Z. Shi, Y. Guo, Y. Tang and Q. Gao, *Adv. Funct. Mater.*, 2016, **26**, 5590–5598.

9 J. Zhang, T. Wang, P. Liu, S. Liu, R. Dong, X. Zhuang, M. Chen and X. Feng, *Energy Environ. Sci.*, 2016, **9**, 2789–2793.

10 H. Wang, S. Min, Q. Wang, D. Li, G. Casillas, C. Ma, Y. Li, Z. Liu, L. J. Li, J. Yuan, M. Antonietti and T. Wu, *ACS Nano*, 2017, **11**, 4358–4364.

11 M. Ledendecker, G. Clavel, M. Antonietti and M. Shalom, *Adv. Funct. Mater.*, 2015, **25**, 393–399.

12 X. Zou, X. Huang, A. Goswami, R. Silva, B. R. Sathe, E. Mikmeková and T. Asefa, *Angew. Chemie*, 2014, **126**, 4461–4465.

13 H. Vrubel and X. Hu, *Angew. Chemie - Int. Ed.*, 2012, **51**, 12703–12706.

14 H. W. Liang, S. Brüller, R. Dong, J. Zhang, X. Feng and K. Müllen, *Nat. Commun.*, 2015, **6**, 1–8.

15 G. Zhou, M. Li, Y. Li, H. Dong, D. Sun, X. Liu, L. Xu, Z. Tian and Y. Tang, *Adv. Funct. Mater.*, 2020, **30**, 1905252.

16 C. Huang, D. Wu, P. Qin, K. Ding, C. Pi, Q. Ruan, H. Song, B. Gao, H. Chen and P. K. Chu, *Nano Energy*, 2020, **73**, 104788.

17 M. R. Liu, Q. L. Hong, Q. H. Li, Y. Du, H. X. Zhang, S. Chen, T. Zhou and J. Zhang, *Adv. Funct. Mater.*, 2018, **28**, 1801136.

18 Z. Chen, R. Wu, Y. Liu, Y. Ha, Y. Guo, D. Sun, M. Liu and F. Fang, *Adv. Mater.*, 2018, **30**, 1802011.

19 X. Zhao, P. Pachfule, S. Li, J. R. J. Simke, J. Schmidt and A. Thomas, *Angew. Chemie - Int. Ed.*, 2018, **57**, 8921–8926.

20 P. P. Liu, H. L. Zhu and Y. Q. Zheng, *J. Mater. Sci.*, 2018, **53**, 11574–11583.

21 H. W. Man, C. S. Tsang, M. M. J. Li, J. Mo, B. Huang, L. Y. S. Lee, Y. chung Leung, K. Y. Wong and S. C. E. Tsang, *Chem. Commun.*, 2018, **54**, 8630–8633.

22 H. Liang, F. Meng, M. Cabán-Acevedo, L. Li, A. Forticaux, L. Xiu, Z. Wang and S. Jin, *Nano Lett.*, 2015, **15**, 1421–1427.

23 N. Jiang, B. You, M. Sheng and Y. Sun, 2015, **54**, 6251–6254.

24 J. Hou, B. Zhang, Z. Li, S. Cao, Y. Sun, Y. Wu, Z. Gao and L. Sun, *ACS Catal.*, 2018, **8**, 4612–4621.

25 M. Li, Z. Xu, Y. Li, J. Wang and Q. Zhong, *Nano Sel.*, 2021, 1–10.

26 L. Gao, X. Cui, Z. Wang, C. D. Sewell, Z. Li, S. Liang, M. Zhang, J. Li, Y. Hu and Z. Lin, *Proc. Natl. Acad. Sci. U. S. A.*,2021, **118**, 1-10.

27 C. Z. Yuan, Z. T. Sun, Y. F. Jiang, Z. K. Yang, N. Jiang, Z. W. Zhao, U. Y. Qazi, W. H. Zhang and A. W. Xu, *Small*, 2017, **13**, 1604161.